

DOI: 10.1002/ ((please add manuscript number))

**Article type: Full Paper**

**Title** In-situ Morphology Studies of the Mechanism for Solution Additive Effects on the Formation of Bulk Heterojunction Films.

Author(s), and Corresponding Author(s)\* *Lee J. Richter,\* Dean A. DeLongchamp,\* Felicia A.*

*Bokel, Sebastian Engmann, Kang Wei Chou, Aram Amassian, Eric Schaible, Alexander*

*Hexemer*

Lee J. Richter, Dean A. DeLongchamp, Felicia A. Bokel, Sebastian Engmann

Material Measurement Laboratory, National Institute of Standards and Technology,

Gaithersburg, Md 20899, USA

E-mail: lee.richter@nist.gov; dean.delongchamp@nist.gov

Kang Wei Chou, Prof. Aram Amassian,

Physical Sciences and Engineering Division, King Abdullah University of Science and

Technology (KAUST) Thuwal 23955-6900, Saudi Arabia

Eric Schaible, Alexander Hexemer, Advanced Light Source,

Lawrence Berkeley National Laboratory, Berkeley, California 94720, USA

Keywords: **organic photovoltaics, organic electronics, X-ray diffraction, SAXS**

The most successful active film morphology in organic photovoltaics is the bulk heterojunction (BHJ). The performance of a BHJ arises from a complex interplay of the spatial organization of the segregated donor and acceptor phases and the local order/quality of the respective phases. These critical morphological features develop dynamically during film formation, and it has become common practice to control them by the introduction of processing additives. We report *in-situ* grazing incidence x-ray diffraction (GIXD) and grazing incidence small angle x-ray scattering (GISAXS) studies of the development of order in BHJ films formed from the donor polymer poly(3-hexylthiophene) and acceptor phenyl-C61-butyric acid methyl ester under the influence of two common additives, 1,8-octanedithiol and 1-chloronaphthalene. By comparing optical aggregation to crystallization and using GISAXS to determine the number and nature of phases present during drying, we arrive at two common mechanisms by which the additives increase P3HT crystallinity. Additives accelerate the appearance of pre-crystalline nuclei by controlling solvent quality and allow for extended crystal growth by delaying the onset of PCBM-induced vitrification. The glass transition effects vary system-to-system and may be correlated to the number and composition of phases present during drying.

## 1. Introduction

Human progress requires a deliberate shift towards sustainable manufacturing, using low-energy fabrication processes and renewable or earth abundant materials.<sup>[1,2]</sup> For photovoltaic panels, the energy recovery time is the length of operation of a panel required to generate the energy used to manufacture the panel. In thin film inorganic panels, this time has dropped to about one year.<sup>[3]</sup> One of the revolutionary appeals of roll-to-roll manufacturing of organic photovoltaics (OPV) is the potential to achieve energy recovery times as low as 10 d.<sup>[4]</sup> Tremendous advances have recently been made in OPV efficiencies,<sup>[5]</sup> all based on optimization of the bulk-heterojunction (BHJ) motif.<sup>[6,7]</sup> The performance of a BHJ requires

the optimization of both its molecular-scale order and its nanometer-scale domain structure.<sup>[8]</sup>

In general, the optimized structure is not at equilibrium. Many techniques have been employed for BHJ film optimization,<sup>[9]</sup> including solvent choice and post deposition thermal<sup>[10]</sup> or vapor annealing.<sup>[11]</sup> Recently, formulations using low volatility liquid additives to achieve higher efficiencies without thermal treatment have become popular.<sup>[12–14]</sup> Although additives such as 1,8-octanedithiol (ODT) and 1-chloronaphthalene (CN) have almost ubiquitous beneficial effects, there is no consensus on either the origin or mechanism of their efficacy. In some systems, additives cause smaller domains,<sup>[15,16]</sup> while in others they cause larger domains.<sup>[12,17]</sup> The efficacy of ODT and diiodooctane has been attributed to selective solvation of the fullerene, enabling improved polymer order. CN, however, is typically a good solvent for both polymer and fullerene and thus must act via a different mechanism.

We recently employed real-time optical techniques to study the mechanism by which the additives ODT and CN influence the solidification of the poly(3-hexylthiophene):phenyl-C61-butyric-acid-methyl-ester (P3HT:PCBM) BHJ.<sup>[18]</sup> Both additives promoted a greater than 5× improvement in device efficiency over the additive-free film in the absence of thermal annealing. Post-deposition characterization with ultraviolet-visible absorption spectroscopy (UV-Vis) and grazing incidence x-ray diffraction (GIXD) established that the additives increased the polymer's local order and crystallinity. Additionally, energy-filtered transmission electron microscopy (EF-TEM) revealed that the morphology changed from very finely mixed to the commonly observed fibrillar P3HT.<sup>[10,19]</sup> The improved device performance was thus attributed to two beneficial effects of the additives, improved local polymer order, resulting in improved hole mobility and a coarsened phase segregation, resulting in less tortuous paths for carrier extraction.

In this earlier work, we used spectroscopic ellipsometry (SE) to track, in real-time, both the film thickness and electronic spectrum (dielectric function). For P3HT, there are clear correlations between the dielectric function and polymer conformation. For brevity, we shall

hereafter refer to optically detected increases in P3HT's local order (its adopting a more regular polymer conformation) as "aggregation". We will present a more detailed discussion of the aggregates later. The decrease of the fluid film thickness was well described by a simple model using Raoult's law, with simultaneous evaporation of the primary solvent (chlorobenzene, CB) and the additive, each having a different constant partial pressure and an evaporation rate determined by its relative presence in the fluid mixture. The fluid film thickness decreased by fast initial evaporation of CB, followed by slower evaporation of the additive. P3HT aggregation in formulations without an additive occurred under conditions of extreme supersaturation; aggregation was not significant until the film was almost dry. This is distinctly different from the near-equilibrium behavior of similar BHJs cast from slowly evaporating dichlorobenzene.<sup>[20]</sup> For ODT-containing formulations, there was virtually no further P3HT aggregation following removal of the CB, consistent with ODT being a non-solvent for P3HT. For CN-containing formulations there was considerable further P3HT aggregation during the CN evaporation. Both additives caused earlier P3HT aggregation, at a lower level of supersaturation. Therefore we proposed that the degradation of solvent quality was a common mechanism of additive influence.

In this paper, we extend our real-time study of the influence of additives in the P3HT/PCBM system with the use of X-ray scattering techniques: GIXD and grazing incidence small angle X-ray scattering (GISAXS). These techniques allow characterization of the *crystalline* order in the film (GIXD) and of the nanoscale phase separation (GISAXS). All films were deposited using a custom blade coater, as shown in Figure 1a. Blade coating is an excellent prototyping method for roll-to-roll coating with a slot-die. Based on the x-ray scattering results, we formulate a hypothesis for the mechanism by which additives improve P3HT crystallinity, incorporating the number and nature of phases present during solidification and the glass transition temperature ( $T_g$ ) within a P3HT-PCBM mixed amorphous phase.

## 2. Results and Discussion

The GIXD technique has seen wide use in the organic semiconductor community as a robust measurement of crystallinity.<sup>[21]</sup> We first consider the GIXD measurement of crystallinity characteristics for dried P3HT:PCBM films. Shown in Figure 1b is a typical, raw GIXD detector image for a P3HT:PCBM film. The primary features are well established:<sup>[22]</sup> a pronounced (h00) diffraction series [typically (100) through (300) are visible] corresponding to the crystalline P3HT lamellar repeat distance (1.69 nm), a weak (010) feature at  $1.6 \text{ \AA}^{-1}$  due to the P3HT  $\pi$ - $\pi$  stacking, and a broad, isotropic feature at  $1.4 \text{ \AA}^{-1}$  attributed to amorphous scattering from glassy PCBM (see Figure S0 for details).

The relative crystallinity of P3HT and its crystal orientation distribution can be determined using pole figures, as shown in Figure 1c. These figures illustrate differences in the (100) packing, and include P3HT/PCBM films formed using different additive formulations. The pole figure maps the diffraction intensity of the (100) peak with the angle  $\Omega$ , which is the angle between the film surface normal and the measured lattice vector (Figure S1).<sup>[23]</sup> The intensity data have been normalized by the film thickness (from spectroscopic reflectometry) and the P3HT volume fraction (calculated from mass loading and density<sup>[24]</sup>). The integrated intensity of the normalized pole figure, properly weighted by solid angle ( $\sin(\Omega)$ ),<sup>[23]</sup> can be used to compare relative P3HT crystallinity and its shape used to compare crystal orientation distribution. The results for the neat P3HT film are similar to those in the literature<sup>[22]</sup> and represent a moderately crystalline film with a significant preference for edge-on order. The full width at half maximum (FWHM) of the pole figure, which we will use for brevity to describe the breadth of the orientation distribution even though there is no *a priori* reason to expect the distribution to have a particular functional peak shape, is about  $36^\circ$ . In comparison, the additive-free BHJ film has significantly lower relative crystallinity, and the ordered

material that is present exhibits significantly greater preference for edge-on orientation with a  $\text{FWHM} \approx 7^\circ$ .

The influence of the two additives on the final film relative crystallinity is displayed Figure 1d, as the integrated, weighted intensity of the orientation scan. Consistent with earlier reports,<sup>[18]</sup> both additives significantly increase the total crystalline fraction. The additives also significantly alter the orientation distribution, restoring the broader components suppressed by the PCBM. The pole figure of the BHJ processed with ODT is very similar to that of the neat polymer ( $\text{FWHM} \approx 27^\circ$ ); however, that of the BHJ processed with CN exhibits a narrower central fraction ( $\text{FWHM} \approx 21^\circ$ ) plus a significant isotropic fraction. In a recent study of order in spun-cast P3HT films, Duong, et al. postulated that one can correlate the orientation distribution in an X-ray diffraction pole figure to the spatial location of crystal nucleation.<sup>[25]</sup> Narrow distributions are attributed to nucleation at a planar interface. This interface could be either the top liquid/air interface or the bottom liquid/solid interface, both are nominally flat during drying. Broader elements in the distribution are attributed to bulk nucleation.<sup>[25]</sup> The additive-free BHJ would, under this framework, be considered to have a significant interface-nucleated fraction due to its narrowness. The broader pole figures in the presence of additives or absence of PCBM suggest a more homogeneous distribution of nucleation sites.

The origins of the improved crystallinity and the altered crystal orientation distributions caused by the additives can be probed by collecting the GIXD during the solidification of the BHJ. Shown in Figure 2 are 2D false color representations of the evolution of the (100) experimental pole figure with time for solidification under 4 conditions: neat P3HT solution, additive-free BHJ solution, BHJ solution with CN, and BHJ solution with ODT. Shown in Figure 3a are the integrated (100) pole figures, derived from Figure 2, and film thickness from simultaneously recorded normal incidence spectral reflectometry. The thickness evolution is consistent with our earlier SE study, with an initial rapid evaporation of the high vapor

pressure primary solvent CB, followed by much slower evaporation of the low-vapor-pressure additive.<sup>[18]</sup> For all systems, the initial appearance of crystallinity occurs very late in the initial stage of drying, under conditions of extreme supersaturation. The solubility limit for P3HT in CB at room temperature is nearly the initial concentration of 20 mg/mL.<sup>[18]</sup> For the neat polymer there is a reproducible decrease in the total crystallinity with sustained measurement of the nominally dry film. This is not due to beam damage because the decrease is not observed for the other systems under much longer viewing times. The physical origin of this decrease is unclear, but it may be related to dissolution or melting of metastable and/or defective crystals because the stage temperature (30 °C) is significantly above the T<sub>g</sub> of the neat polymer (9 °C).<sup>[26,27]</sup> In the additive-free BHJ film, the evolution of crystallinity ends when the CB evaporation ends. Its crystallinity is low, at least lower than that of the neat P3HT film, but it does not further evolve at 30 °C, which suggests that the T<sub>g</sub> of disordered regions is significantly higher than the neat polymer. We will address the issue of glass transition further below.

Additional insight into the drying process can be gained by analyzing the diffraction pattern shape. Shown in Figure 3b is a radially averaged ( $\pm 18^\circ$  sector) diffraction pattern of the final dry films, with the scattering vector  $q$  nominally perpendicular to the substrate ( $q_x \sim 0$ ), such that it describes the characteristics of crystal planes parallel to the substrate. The (100) feature, which describes the regular layering of the P3HT chains, was fit to a Lorentzian and a linear background. The peak position and FWHM <sub>$q$</sub>  were extracted as a function of time. The resultant fit parameters are shown in Figures 3c and 3d. The FWHM <sub>$q$</sub>  can be related to a characteristic grain size (in the lamellar repeat direction) based on the Scherrer relationship ( $d_{\text{grain}} \approx 2\pi/\text{FWHM}_q$ ). Because defects within domains can broaden the FWHM <sub>$q$</sub> , the Scherrer grain size should be considered a coherence length, i.e. a convolution of crystal size and quality. Except for the ODT processed film, there is very little variation in  $d_{\text{grain}}$  with time. In

the case of ODT, there is a slight increase in  $d_{\text{grain}}$  during the final stage of additive evaporation. The neat polymer and the two additive processed BHJs exhibit similar  $d_{\text{grain}}$  ( $\approx 8.9$  nm) at the end of drying. The largest  $d_{\text{grain}}$  ( $\approx 13$  nm) is found for the interface nucleated crystals in the additive-free BHJ. Also shown in Figure 3d is the (100) peak position. As has been reported for thermal annealing of P3HT<sup>[22,28]</sup> there is a consistent decrease in layer spacing (increase in  $q$ ) with increasing crystalline content seen for all films. The final (100) layer spacing is nominally the same for all films:  $\approx 1.6$  nm.

The GIXD results present a simple picture for the influence of the additives. The presence of PCBM significantly inhibits the development of misoriented (likely bulk-nucleated) crystallites with respect to the neat polymer. Both additives restore the population of bulk-nucleated crystallites. The presence of PCBM appears to inhibit P3HT bulk crystallization but does not significantly inhibit interface nucleation. This is supported by angle-of-incidence dependent pole figures (S2) provided in the supplemental information. Broad, isotropic contributions to the orientation distribution are only seen at incidence angles larger than the critical angle for the film, characteristic of the film interior. The appearance of only a narrow fraction at lower incidence angles indicates that interface nucleation occurs at the top of the film (the flat air/liquid interface).

It is important to ascertain how PCBM suppresses the P3HT bulk crystallization. It has been proposed<sup>[12]</sup> that early solidification of the fullerene creates a PCBM network that inhibits the development of P3HT crystallinity. We propose an alternative explanation, based on the recent discovery that amorphous PCBM is miscible in the amorphous regions of P3HT and most other semiconducting polymers.<sup>[29–31]</sup> The  $T_g$  of a mixed amorphous phase containing both P3HT and PCBM should lie between the  $T_g$  of the neat polymer and the  $T_g$ , 118 °C, of pure PCBM.<sup>[26,27]</sup> As the crystalline P3HT rejects PCBM,<sup>[22]</sup> the mixed amorphous phase should be rich in fullerene (exhibit a higher  $T_g$ ) relative to expectation based on the film mass

ratio. Empirically, 1:1 by mass films exhibit a  $T_g$  for the mixed amorphous regions of  $\approx 60$  °C.<sup>[26,27]</sup> The increased  $T_g$  of the mixed amorphous phase may suppress the crystallization of P3HT during drying because the temperature/solvation coordinate quickly passes below it. We will describe this hypothesis as vitrification,<sup>[32]</sup> which is by definition the transition of a liquid to a glass as it passes below  $T_g$ . The top surface is nearly pure P3HT<sup>[33]</sup> and therefore its  $T_g$  is likely to be significantly lower. Additionally, the interface-nucleated, orientationally-narrow fraction crystallizes early while significant solvent is still present.

This vitrification hypothesis is consistent with recent *in-situ* studies of the slow (near equilibrium) drying of P3HT/PCBM BHJs from DCB solutions. For this system, the development of P3HT crystals and PCBM solidification are separated in time and the PCBM solidification clearly occurs after polymer ordering.<sup>[20]</sup> This hypothesis is also consistent with the PCBM concentration dependence of the P3HT (100) pole figure, shown in S3. At PCBM mass fraction  $\leq 40$  %, where  $T_g$  of the mixed amorphous material is below the stage temperature, there is very little perturbation of the P3HT crystallinity. To extend this hypothesis to additives, we propose that the additives lower the  $T_g$  of the mixed amorphous phase, allowing crystallization to occur at a far lower temperature/solvation coordinate, hence restoring the bulk crystallization that PCBM inhibits. There are at least two potential ways the additives could lower the  $T_g$  of the mixed amorphous phase: 1) by direct plasticization of that phase or 2) by removing the high- $T_g$  PCBM to a second amorphous phase via selective solvation. We address these possibilities later in this manuscript.

The GIXD evolution of the ODT additive P3HT/PCBM films is in stark contrast with our earlier optical studies.<sup>[18]</sup> In the optical studies, P3HT aggregation, as judged by the normalized height of the 0-0 feature in the Franck-Condon envelope, ceased to evolve when the primary solvent (CB) finished evaporating from the film (near 20 s). However, in the GIXD, the film continues to evolve over the entire time that the film is swollen with the additive (20 to 300) s. This is illustrated in Figure4 in which p-polarized, near Brewster's

angle transmission studies are contrasted with the above GIXD results. The experiments were performed on independent films in different labs, and therefore the timings are not identical. No attempt was made to scale the results, however the comparison is clear. In the case of the additive-free film, both the polymer spectrum and the GIXD cease to evolve abruptly upon removal of the CB. In the case of the CN additive, both the UV-Vis spectrum and the GIXD evolve continuously as the CN-swollen film dries. However, in the case of the ODT additive, the evolution of the absorption spectrum ends abruptly while there is extensive continuing growth in the GIXD pattern.

We propose the following resolution of the apparent uncorrelated optical order and diffraction order in the drying BHJ film. The optical order in P3HT can be quantitatively interpreted in terms of a weakly coupled H-aggregate model. The relative height of the 0-0 feature in the absorption is related to the inter-chain bandwidth,<sup>[34]</sup> which is inversely related to the conjugation length along the polymer chain, c-axis.<sup>[35]</sup> The optically measured aggregation therefore relates to local c-axis order, whereas crystallization, as monitored by the (100) peak intensity, relates to the lamellar, or a-axis, order. Previous comparisons of optical measurements to diffraction measurements show that they are often uncorrelated.<sup>[36]</sup>

Kinetically, aggregation clearly precedes crystallization, and we therefore attribute the aggregated state to the formation of pre-crystalline nuclei. Our earlier optical study found a direct correlation between the extent of aggregation and the concentration at the onset of ordering. Additives promoted earlier aggregation, attributed to degradation of the solvent quality. In the current study, we see that *crystallization* occurs the entire time the film is swollen with ODT, possibly because the additive lowers the T<sub>g</sub> of the mixed amorphous phase. This suggests that the additives have two mechanisms of action: 1) they lower solvent quality, accelerating the early formation of pre-crystalline aggregates, and 2) they lower the T<sub>g</sub> of the mixed amorphous phase allowing for prolonged crystallization late in drying.

The GISAXS method provides insight into the characteristic length scales of domains in the BHJ. Shown in Figure 5 is a representative GISAXS pattern recorded at the end of a dynamic study of film deposition. Following Gomez and co-workers<sup>[37]</sup> we have analyzed the GISAXS, within the Born approximation, by constructing  $q^2$  weighted scattering functions only from the enhanced scattering in the  $q_z=0$  plane due to wave guiding of the totally internally reflected beam. Representative data are shown in Figure 5b. The results are consistent with earlier reports of GISAXS from P3HT.<sup>[37-39]</sup> There is a single peak in the scattering at  $q_0$  corresponding to a characteristic dimension of  $\approx 28$  nm. The most significant difference in the films is the total scattering invariant ( $TSI = \int I q^2 dq$ ), that increases significantly when additive is present. There is also evidence for a low  $q$ -tail in the additive processed films. To reconcile these results with previously published energy-filtered TEM<sup>[18,40]</sup> we attribute the single peak to the characteristic separation of P3HT crystalline regions and the tail to the long dimension of the fibrils, characteristic of the additive processed films. It is interesting to note the strong similarity between the GISAXS patterns and small angle neutron scattering results for P3HT and P3HT/PCBM gels.<sup>[41,42]</sup> Shown in Figure 6 are summaries of the TSI and the peak location (reported as  $r_0 = 2\pi/q_0$ ) for the three BHJ films. Also shown is the film thickness from the simultaneously recorded reflectometry. The evolution of the GISAXS is similar to that of the Figure 3 P3HT (100) integrated pole figure, indicating that the BHJ domain development is driven by P3HT crystallization. In the absence of additives, both  $q_0$  and the TSI develop under conditions of extreme supersaturation and stop evolving upon the complete removal of CB. In the presence of both additives, there is a significant increase in the TSI during the late-time (after CB removal) drying of the additive-swollen film.

To further analyze the late-time evolution of the GISAXS in the additive-swollen films, we must consider the number and nature of phases that could form domains. It is well established that there is negligible solubility of PCBM in P3HT crystals,<sup>[22]</sup> so the simplest BHJ model would include two phases: 1) P3HT crystals and 2) a mixed amorphous phase containing

amorphous P3HT, the large scattering length density (SLD) PCBM, and the additive. A significant contribution to the TSI evolution can be attributed to contrast changes due to the evaporation of the low-SLD additive. As shown in Figure 7, a two-phase model well describes the evolution of the TSI for the CN additive (see supplemental for details). This strongly suggests the presence of only 2 majority phases: crystalline P3HT and a mixed amorphous phase. The significant presence of a separate pure PCBM phase with a characteristic length scale within the  $q$  range studied (.003 to .2)  $1/\text{\AA}$  would disrupt this agreement. However, as seen in Figure 7, this simple 2 phase model does not well describe the evolution of the TSI for the ODT additive. This is not surprising, given the poor solubility of P3HT in ODT. A model containing 3 phases: 1) crystalline P3HT, 2) mixed amorphous P3HT and PCBM, and 3) mixed additive and PCBM describes the data well (see Figure 7). The fit reveals a partition coefficient of PCBM between the additive and amorphous polymer phases that shows a weak preference for the amorphous polymer phase. Models that include complete partitioning of the PCBM into the ODT phase are incompatible with the data. Note that, consistent with the similar final GISAXS patterns (Figure 6), the dry 3 phase model corresponds to only the crystalline polymer and a single mixed amorphous phase as the PCBM repartitions into the mixed phase upon removal of the additive.

The evolution of  $r_0$  is in interesting contrast to the TSI. In the case of ODT there is a factor of 2 decrease in the characteristic polymer-polymer correlation length with time, consistent with deswelling of a fiber matrix by removal of the insoluble additive. This implies early aggregation of the complete polymer matrix (consistent with the optical data) followed by crystallization of the fibers upon removal of the non-solvent. In the case of CN, there is very little evolution of  $r_0$ . This would suggest that the CN film develops by continuous nucleation of new ordered regions (with nominally fixed correlations due to tie chains) out of the CN-solvated bulk, again, consistent with the continuous evolution of the optical data.

The evolution of structure in the OPV films we studied is summarized in Figure 8. The evaporation regimes of each liquid are determined from the liquid film thickness measurements. The local order is determined by the SE methods described in our earlier publication, where the onset of local order change marks the point where the optical spectrum begins to deviate from that of the solution, and the end of local order change marks the point where the optical spectrum ceases to change. The long range order was measured by GIXD, and the domain formation by GISAXS, as we describe above. For these scattering measurements, the onset and end roughly mark the times where first scattering is observed and the pattern ceases to change, respectively. Qualitative judgments about the speed of change in different time regimes are also included for illustrative purposes.

The number and nature of phases in each of the drying films are described in the summaries. The additive-free CB solution is summarized in Figure 8a. It dries quickly, and the local order, long-range order, and domain formation all occur roughly simultaneously within the last few seconds of CB evaporation. We interpret this as the crystallization of P3HT from a homogeneous solution of P3HT and fullerene in CB. Once sufficient CB is removed such that crystallization ceases, the remaining polymer and all of the fullerene are left as a mixed amorphous glass.

The solution with CN additive is summarized in Figure 8b. It exhibits an early, fast solidification regime where the local order and long-range order co-evolve near the end of CB evaporation. We interpret this first step as P3HT crystallization similar to that of the additive-free solution. The two phases remaining after CB is evaporated are 1) the P3HT crystal and 2) a CN solution of P3HT and PCBM. Given the small amount of CN relative to the P3HT and PCBM, this second phase is perhaps better described as a CN-plasticized mixed amorphous phase of P3HT and PCBM. A second, slower P3HT crystallization is observed as the CN evaporates. Once the CN is fully evaporated, the uncrystallized P3HT and the PCBM remain as a mixed amorphous phase.

The solution with ODT additive, as summarized in Figure 8c, exhibits the most complex behavior. As was observed in the other two systems, an early rapid P3HT crystallization occurs near the end of CB evaporation. After the CB is left, our modeling described above suggests that 3 phases remain: 1) P3HT crystal, 2) an ODT solution of PCBM, and 3) a P3HT/PCBM mixed phase. The PCBM is partitioned between the two PCBM-containing phases by a constant coefficient. At early times during this second drying regime, the ODT volume is large relative to the amorphous P3HT volume, and therefore most of the PCBM resides in the ODT phase. As the ODT dries, the P3HT further crystallizes. At the same time, the PCBM moves out of the ODT-containing liquid phase and into the P3HT/PCBM mixed amorphous phase due to the shrinking volume of ODT and the constant partition coefficient. As the ODT volume becomes vanishingly small, the last PCBM molecules move into the P3HT/PCBM mixed amorphous phase and the ODT/PCBM phase disappears, leaving behind only crystalline P3HT and a mixed amorphous phase.

### 3. Conclusion

From our combination of real-time measurement results, a consensus model for the development of order in the P3HT:PCBM system emerges. The normal crystallization of the polymer is disrupted by the PCBM, due to the relatively high  $T_g$  of the P3HT/PCBM glass, which cannot further evolve P3HT crystals at room temperature after the removal of CB. In the case of the CN additive, the P3HT continues to prodigiously crystallize after CB removal from a CN-plasticized mixed amorphous P3HT/PCBM phase having lowered  $T_g$ . In the case of the ODT additive, two liquid/amorphous phases are formed, and PCBM is removed from the P3HT-rich phase into ODT, lowering the  $T_g$  of the P3HT-rich phase. It is also possible that ODT could directly plasticize P3HT, if a trace amount of it partitions into that phase. Only the ODT mechanism requires the additive to be a selective solvent for the PCBM. In

particular ODT's immiscibility with P3HT is the basis for the formation of a second liquid phase partitioning fullerene away from P3HT.

#### 4. Experimental Section

All films were prepared using the blade-coating technique,<sup>[43]</sup> as previously described.<sup>[18]</sup> In brief, the BHJ master solution was a 1:1 (by mass) mixture of P3HT (OS 2100, Plextronics Inc.)<sup>[44]</sup> and PCBM (Nano-C) well-dissolved in chlorobenzene (CB) at 40 mg/mL (total solids) concentration at 70 °C. Additive solutions were prepared by addition of 2 % (by volume with respect to CB) of ODT and CN. Approximately 20 µL of the P3HT:PCBM solution was dispensed from a 70 °C syringe under the edge of a glass blade fixed at 300 µm above the substrate surface. The substrate temperature was 30 °C. The blade was immediately translated at 10 mm/s of velocity. The final BHJ film ellipsometric thickness was nominally 150 nm. The substrate was fixed and the knife blade translated. Care was taken to orient the blade translation direction parallel to the sample stage of the instrument to avoid any possible thickness gradient. All films were prepared on PEDOT:PSS treated Si substrates to closely mimic device films.

*In-situ* x-ray scattering measurements were performed at the Advanced Light Source<sup>[45]</sup> beam line 7-3-3, with a beam energy of 10 keV. For GIXD measurements a 2D image detector (Dectris Pilatus 1M) was located at a distance of ca. 280 mm from the sample center. The measurements were performed in ambient air to reproduce the drying conditions of earlier studies.<sup>[18]</sup> Slits were adjusted to produce a nominally 0.3 mm high beam which overfilled the nominally 2 cm wide substrate. *In-situ* GISAXS was performed at the same beam line with the 2D image detector-to-sample distance 3850 mm. An evacuated flight tube was used to minimize air scatter. The x-ray beam was attenuated to eliminate sample damage. The detector was calibrated with a silver behenate standard. Both GIXD and GISAXS data was reduced with the Nika software package.<sup>[46]</sup> Simultaneous with both GIXD and GISAXS

measurements, normal incidence spectral reflectometry was performed with a home-made, fiber spectrometer based system. Care was taken to overlap the reflectometry probe beam ( $\approx 0.3$  mm diameter) with the stripe illuminated by x-rays. The reflectometry was analyzed using a commercial ellipsometry code (JA Woollam WVASE32). X-ray data were recorded with a variable integration time and period. The initial 120 s were recorded at  $\approx 0.1$  s integration and period while the next (3 to 8) min were recorded with 1 s integration and 1.5 s period. The reflectometry was recorded at a constant  $\approx 0.1$  s integration and period.

*In-situ* p-polarized, near-Brewster transmission data were acquired with an M-2000DI series spectroscopic ellipsometer (J.A. Woollam Inc.) at fixed  $45^\circ$  of incidence angle with respect to the surface normal. The weakly focused beam was nominally  $0.3$  mm  $\times$   $0.9$  mm on the sample. A PEDOT:PSS coated quartz substrate was mounted on a sample stage that has a hole with a diameter of  $\approx 24$  mm. The UV-Vis beam was p-polarized and aligned to penetrate the sample and bounce up to the detector.

### **Supporting Information**

Supplementary information, defining the experimental GIWAXS angles and their relationship to the proper scattering angle  $\Omega$ , presenting the angle-of-incidence dependence of the (100) pseudo pole figure, comparing crystallinity with PCBM loading and modeling the TSI based on the (100) pole figure is available from the Wiley Online Library or from the authors LJR or DMD.

**Acknowledgements**

The authors wish to thank Jacqueline Johnson and Edwin Chan for assistance in the development of the remote dispense system. Beamline 7.3.3 of the Advanced Light Source is supported by the Director of the Office of Science, Office of Basic Energy Sciences, of the U.S. Department of Energy under Contract No. DE-AC02-05CH11231.

Received: ((will be filled in by the editorial staff))

Revised: ((will be filled in by the editorial staff))

Published online: ((will be filled in by the editorial staff))

- [1] M. L. Green, L. Espinal, E. Traversa, E. J. Amis, *MRS Bull.* **2012**, *37*, 303.
- [2] L. M. Peter, *Philos. Trans. R. Soc. A: Math. Phys. Eng. Sci.* **2011**, *368*, 1840.
- [3] F. C. Krebs, *Sol. Energy Mater. Sol. Cells* **2009**, *93*, 394.
- [4] R. Sondergaard, M. Hosel, D. Angmo, T. T. Larsen-Olsen, F. C. Krebs, *Mater. Today* **2012**, *15*, 36.
- [5] M. A. Green, K. Emery, Y. Hishikawa, W. Warta, E. D. Dunlop, *Prog. Photovoltaics: Res. Appl.* **2013**, *21*, 827.
- [6] G. Yu, J. Gao, J. C. Hummelen, F. Wudl, A. J. Heeger, *science* **1995**, *270*, 1789.
- [7] G. Dennler, M. C. Scharber, C. J. Brabec, *Adv. Mater.* **2009**, *21*, 1323.
- [8] D. M. DeLongchamp, R. J. Kline, A. Herzing, *Energy & Environ. Sci.* **2012**, *5*, 5980.
- [9] G. Li, V. Shrotriya, Y. Yao, J. Huang, Y. Yang, *J. Mater. Chem.* **2007**, *17*, 3126.
- [10] S. Berson, R. De Bettignies, S. Bailly, S. Guillerez, *Adv. Funct. Mater.* **2007**, *17*, 1377.
- [11] G. Li, V. Shrotriya, J. Huang, Y. Yao, T. Moriarty, K. Emery, Y. Yang, *Nat. Mater.* **2005**, *4*, 864.
- [12] J. Peet, J. Y. Kim, N. E. Coates, W. L. Ma, D. Moses, A. J. Heeger, G. C. Bazan, *Nat. Mater.* **2007**, *6*, 497.
- [13] A. J. Moulé, K. Meerholz, *Adv. Funct. Mater.* **2009**, *19*, 3028.
- [14] H.-C. Liao, C.-C. Ho, C.-Y. Chang, M.-H. Jao, S. B. Darling, W.-F. Su, *Mater. Today*

2013, 16, 326.

- [15] J. S. Moon, C. J. Takacs, S. Cho, R. C. Coffin, H. Kim, G. C. Bazan, A. J. Heeger, *Nano Lett.* **2010**, 10, 4005.
- [16] Y. Liang, Z. Xu, J. Xia, S.-T. Tsai, Y. Wu, G. Li, C. Ray, L. Yu, *Adv. Mater.* **2010**, 22, 135.
- [17] H.-Y. Chen, H. Yang, G. Yang, S. Sista, R. Zadoyan, G. Li, Y. Yang, *J. Phys. Chem. C* **2009**, 113, 7946.
- [18] N. Shin, L. J. Richter, A. A. Herzing, R. J. Kline, D. M. DeLongchamp, *Adv. Energy Mater.* **2013**, 3, 938.
- [19] A. J. Moulé, K. Meerholz, *Adv. Mater.* **2008**, 20, 240.
- [20] B. Schmidt-Hansberg, M. Sanyal, M. F. G. Klein, M. Pfaff, N. Schnabel, S. Jaiser, A. Vorobiev, E. Müller, A. Colsmann, P. Scharfer, D. Gerthsen, U. Lemmer, E. Barrena, W. Schabel, *ACS Nano* **2011**, 5, 8579.
- [21] J. Rivnay, S. C. B. Mannsfeld, C. E. Miller, A. Salleo, M. F. Toney, *Chem. Rev.* **2012**, 112, 5488.
- [22] E. Verploegen, R. Mondal, C. J. Bettinger, S. Sok, M. F. Toney, Z. Bao, *Adv. Funct. Mater.* **2010**, 20, 3519.
- [23] J. L. Baker, L. H. Jimison, S. Mannsfeld, S. Volkman, S. Yin, V. Subramanian, A. Salleo, A. P. Alivisatos, M. F. Toney, *Langmuir* **2010**, 26, 9146.
- [24] H. W. Ro, B. Akgun, B. T. O'Connor, M. Hammond, R. J. Kline, C. R. Snyder, S. K. Satija, A. L. Ayzner, M. F. Toney, C. L. Soles, D. M. DeLongchamp, *Macromolecules* **2012**, 45, 6587.
- [25] D. T. Duong, M. F. Toney, A. Salleo, *Phys. Rev. B* **2012**, 86.
- [26] T. T. Ngo, D. N. Nguyen, *Adv. Nat. Sci. Nanosci. Nanotechnol.* **2012**, 3.
- [27] J. Y. Kim, C. D. Frisbie, *J. Phys. Chem. C* **2008**, 112, 17726.
- [28] S. Hugger, R. Thomann, T. Heinzl, T. Thurn-Albrecht, *Colloid Polym. Sci.* **2004**, 282.

- [29] N. D. Treat, M. A. Brady, G. Smith, M. F. Toney, E. J. Kramer, C. J. Hawker, M. L. Chabiny, *Adv. Energy Mater.* **2011**, *1*, 82.
- [30] B. A. Collins, J. R. Tumbleston, H. Ade, *J. Phys. Chem. Lett.* **2011**, *2*, 3135.
- [31] B. A. Collins, E. Gann, L. Guignard, X. He, C. R. McNeill, H. Ade, *J. Phys. Chem. Lett.* **2010**, *1*, 3160.
- [32] P. Westacott, J. R. Tumbleston, S. Shoaee, S. Fearn, J. H. Bannock, J. B. Gilchrist, S. Heutz, J. deMello, M. Heeney, H. Ade, J. Durrant, D. S. McPhail, N. Stingelin, *Energy & Environ. Sci.* **2013**, *6*, 2756.
- [33] D. S. Germack, C. K. Chan, R. J. Kline, D. A. Fischer, D. J. Gundlach, M. F. Toney, L. J. Richter, D. M. DeLongchamp, *Macromolecules* **2010**, *43*, 3828.
- [34] F. C. Spano, *J. Chem. Phys.* **2005**, *122*, 234701.
- [35] J. Gierschner, Y.-S. Huang, B. V. Averbek, J. Cornil, R. H. Friend, D. Beljonne, *J. Chem. Phys.* **2009**, *130*, 044105.
- [36] M. Sanyal, B. Schmidt-Hansberg, M. F. G. Klein, A. Colmann, C. Munuera, A. Vorobiev, U. Lemmer, W. Schabel, H. Dosch, E. Barrena, *Adv. Energy Mater.* **2011**, *1*, 363.
- [37] D. R. Kozub, K. Vakhshouri, L. M. Orme, C. Wang, A. Hexemer, E. D. Gomez, *Macromolecules* **2011**, *44*, 5722.
- [38] S. V. Kesava, R. Dhankar, D. R. Kozub, K. Vakhshouri, U. H. Choi, R. H. Colby, C. Wang, A. Hexemer, N. C. Giebink, E. D. Gomez, *Chem. Mater.* **2013**, *25*, 2812.
- [39] H.-C. Liao, C.-S. Tsao, T.-H. Lin, C.-M. Chuang, C.-Y. Chen, U.-S. Jeng, C.-H. Su, Y.-F. Chen, W.-F. Su, *J. Am. Chem. Soc.* **2011**, *133*, 13064.
- [40] A. A. Herzing, L. J. Richter, I. M. Anderson, *J. Phys. Chem. C* **2010**, *114*, 17501.
- [41] G. M. Newbloom, F. S. Kim, S. A. Jenekhe, D. C. Pozzo, *Macromolecules* **2011**, *44*, 3801.
- [42] M. J. Sobkowicz, R. L. Jones, R. J. Kline, D. M. DeLongchamp, *Macromolecules* **2012**, *45*, 1046.

[43] C. M. Stafford, K. E. Roskov, T. H. Epps, M. J. Fasolka, *Rev. Sci. instruments* **2006**, *77*, 023908.

[44] Certain commercial equipment, instruments, or materials are identified in this paper in order to specify the experimental procedure adequately. Such identification is not intended to imply recommendation or endorsement by the National Institute of Standards and Technology, nor is it intended to imply that the materials or equipment identified are necessarily the best available for the purpose.

[45] A. Hexemer, W. Bras, J. Glossinger, E. Schaible, E. Gann, R. Kirian, A. MacDowell, M. Church, B. Rude, H. Padmore, *J. Physics: Conf. Ser.* **2010**, *247*, 012007.

[46] J. Ilavsky, *J. Appl. Crystallogr.* **2012**, *45*, 324.

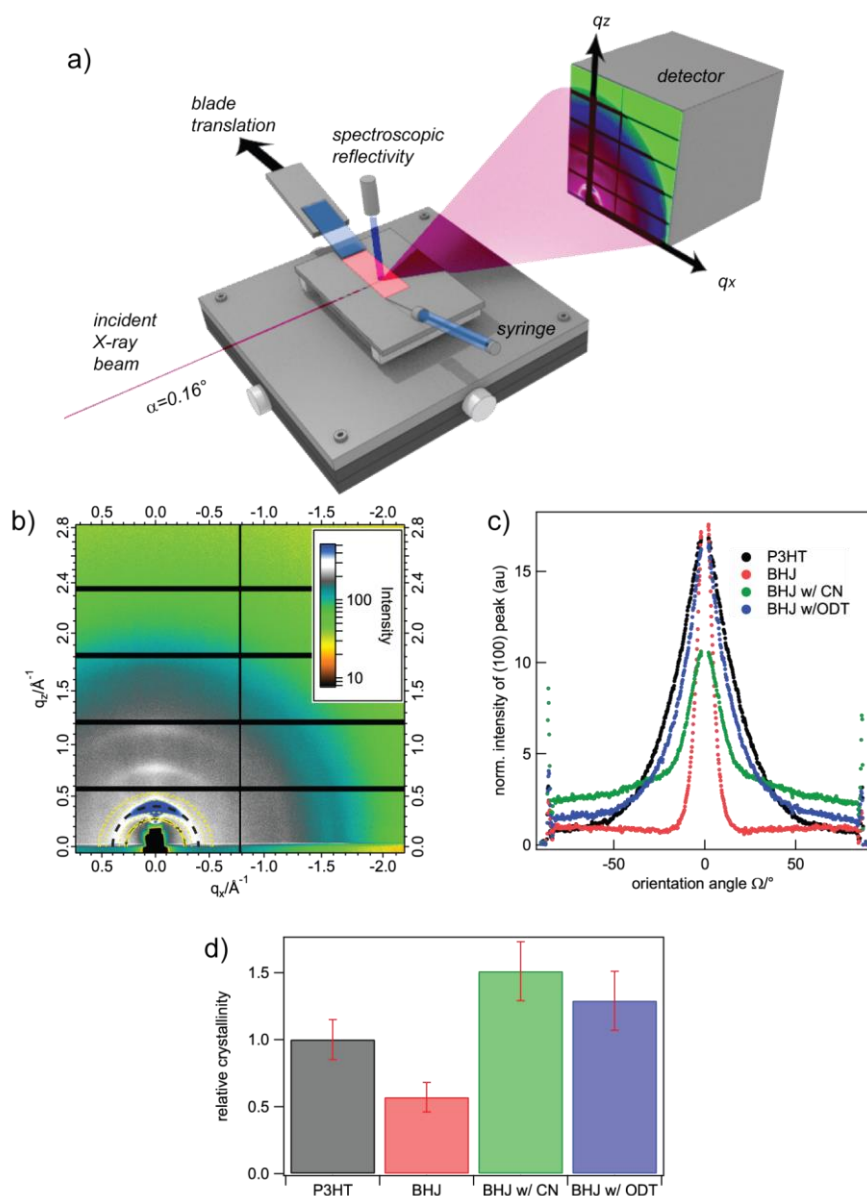


**Figure 1.** a) Schematic view of experiment. b) Experimental GIXD detector image for a neat P3HT film, vs uncorrected momentum transfer:  $q$ , recorded at the critical angle. Dashed lines show regions used to define the (100) and background. c) Background corrected pole figure for (100); data have been normalized for both film thickness and polymer volume fraction. A small gap near  $90^\circ$  arises from a correction to the scattering angle due to the small fixed incidence angle d) Relative crystallinity from orientation scan integrals. Error bars are one standard deviation over 3 or 4 duplicate films.

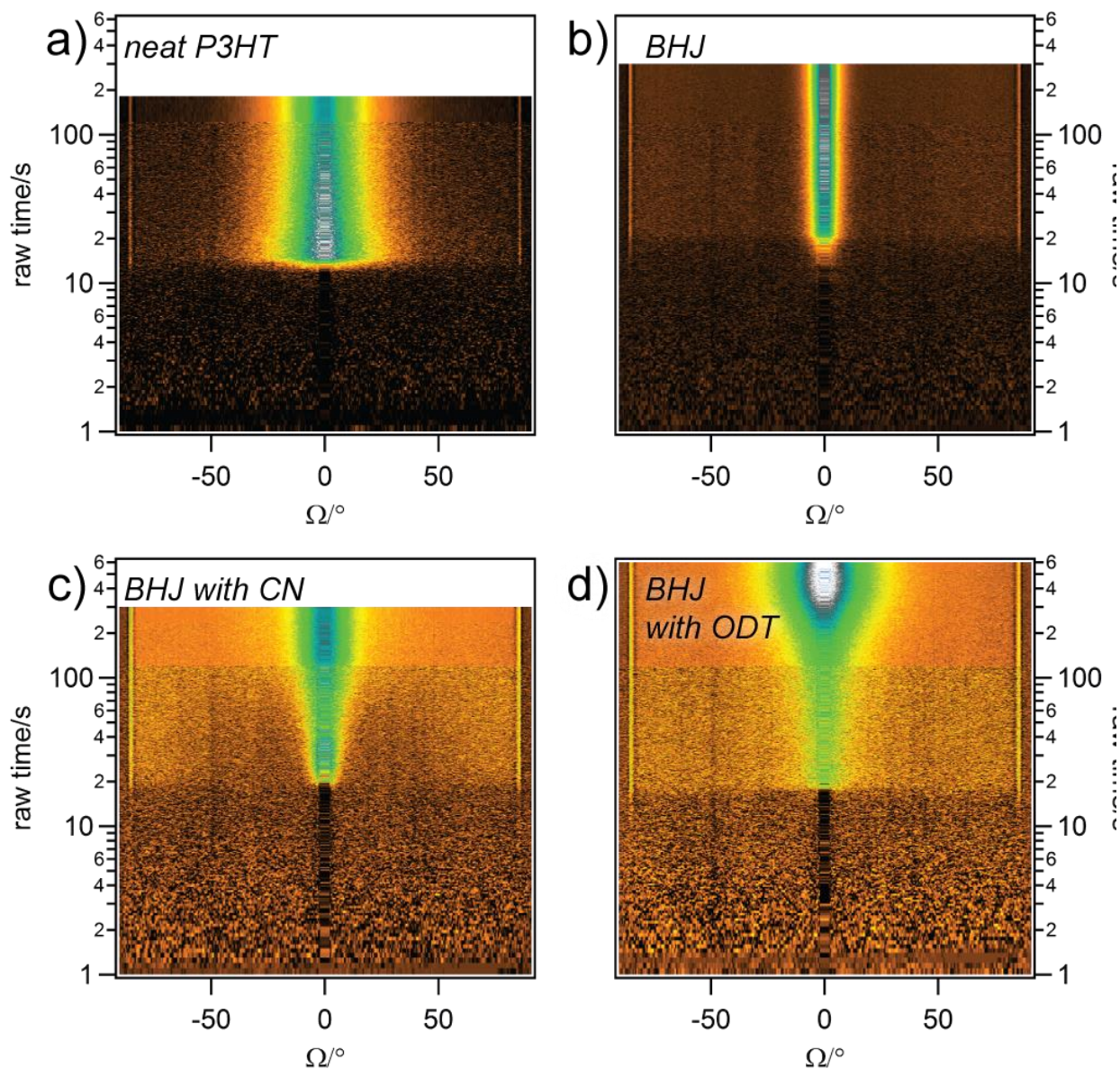


**Figure 2.** 2D false color images of radially averaged and background corrected (100) diffraction intensity vs time. a) neat P3HT film; b) additive-free BHJ film; c) BHJ film with CN additive; d) BHJ film with ODT additive. All data were recorded for beam incidence at  $0.03^\circ$  to  $0.05^\circ$  greater than the film critical angle. The change in background uniformity at approximately 15 s is due to increased reflectivity upon evaporation of the CB, while the change at 120 s is due to improved counting statistics upon increasing the integration time from 0.095 s to 1.0 s.

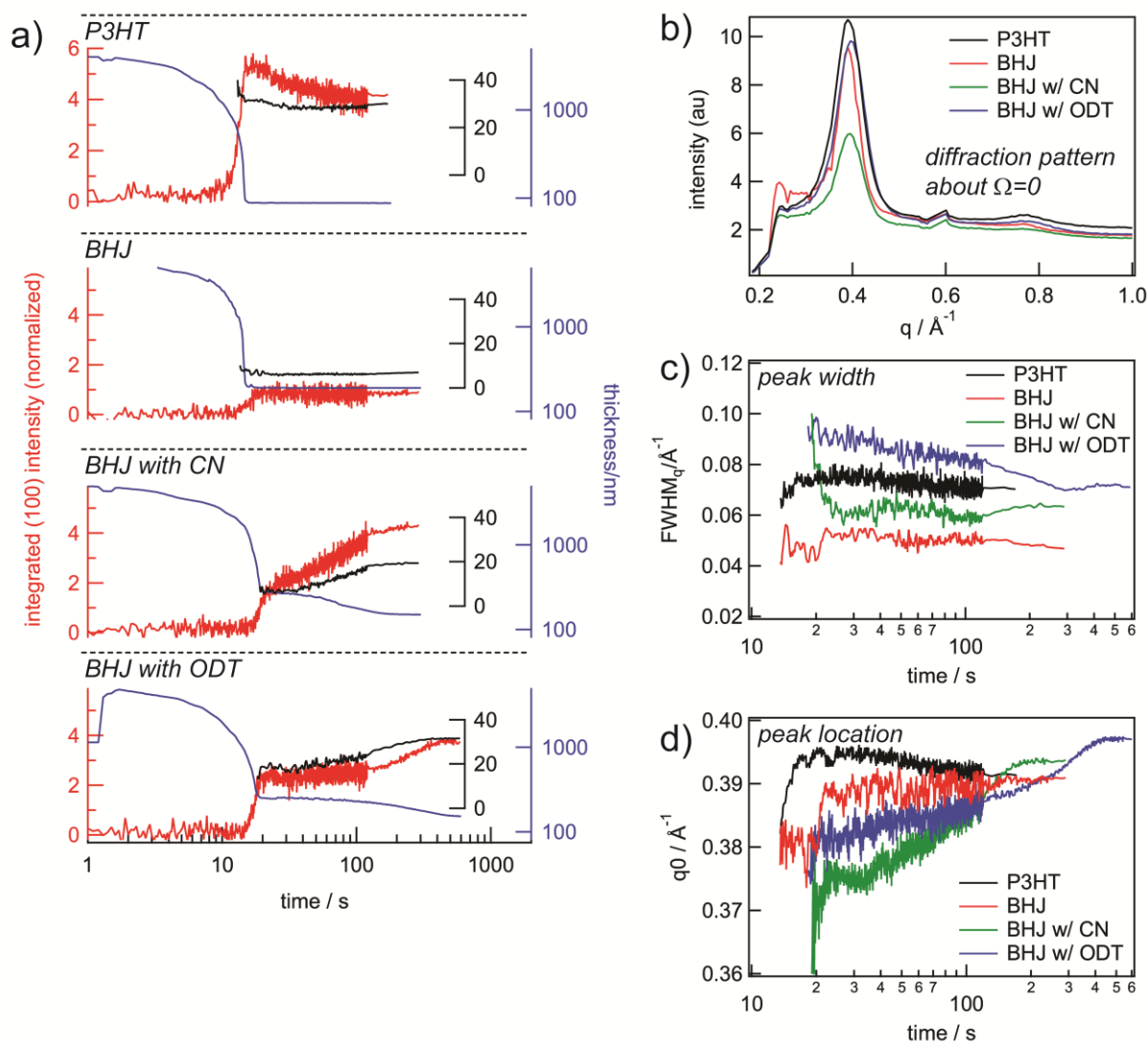


Figure 3. a) Time dependence of: red- Integrated (100) pole figure intensity (normalized by final film thickness and polymer volume fraction); black- FWHM (in  $^\circ$ ) of (100) pole figure; blue- film thickness. b) sector-averaged data around  $\Omega=0$ ; c) FWHM<sub>q</sub> of (100) feature in sector average d) (100) peak location.

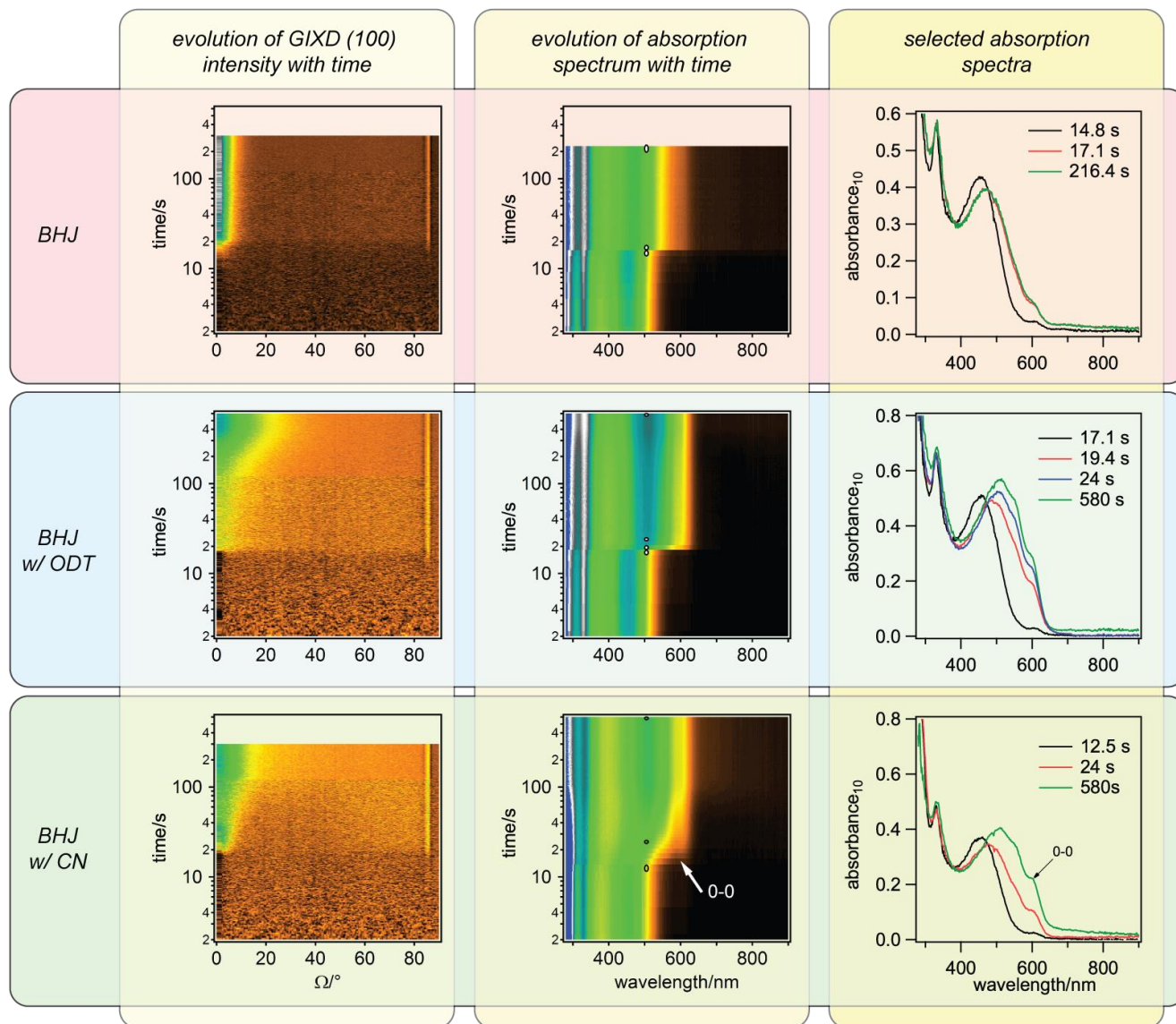


Figure 4. Comparison of time evolution of GIXD pole figure (left) and p-polarized near-Brewster transmission spectroscopy (center). Select spectra are shown from the indicated times on the right. The 0-0 component of the Franck-Condon series is indicated in the CN transmission spectra. Experiments were conducted independently, so small differences in timing due to variations in drying rate and initial film thickness are present.

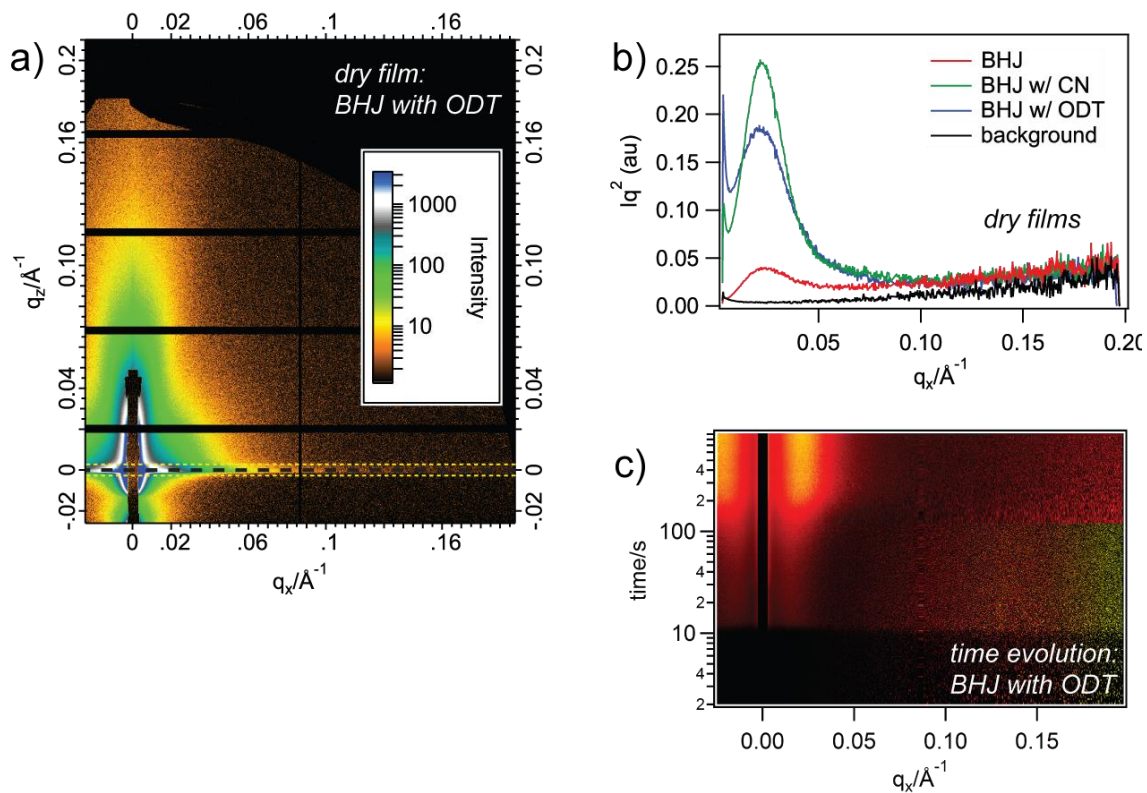


Figure 5. a) GISAXS detector image from a BHJ film deposited from an ODT volume fraction 2 % solution. b)  $I(q_z=0)q_x^2$  for dry BHJ films, extracted along the evanescent field enhanced horizon. c) False color plot of  $I(q_z=0)q_x^2$  for the ODT containing solution as a function of time.

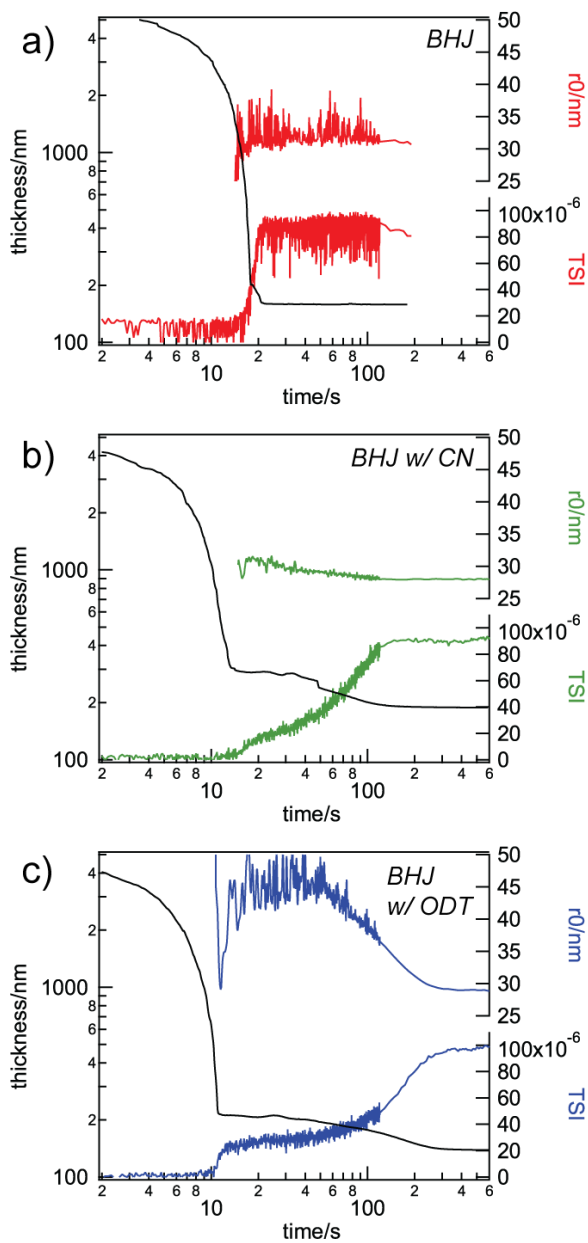


Figure 6. Summary of time-resolved GISAXS results (TSI and  $r_0$ ) for BHJ solutions with a) no additive, b) CN volume fraction 2 %, c) ODT volume fraction 2 %. Simultaneously determined thickness is also shown in black.

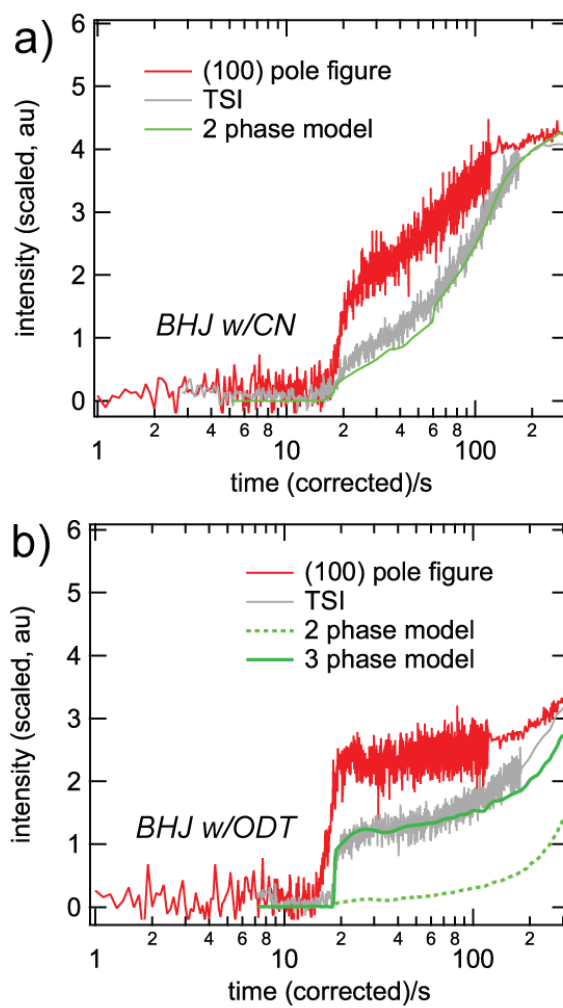


Figure 7 Comparison of TSI and TSI computed from simple 2 phase and 3 phase models for a) CN- and b) ODT-containing films.

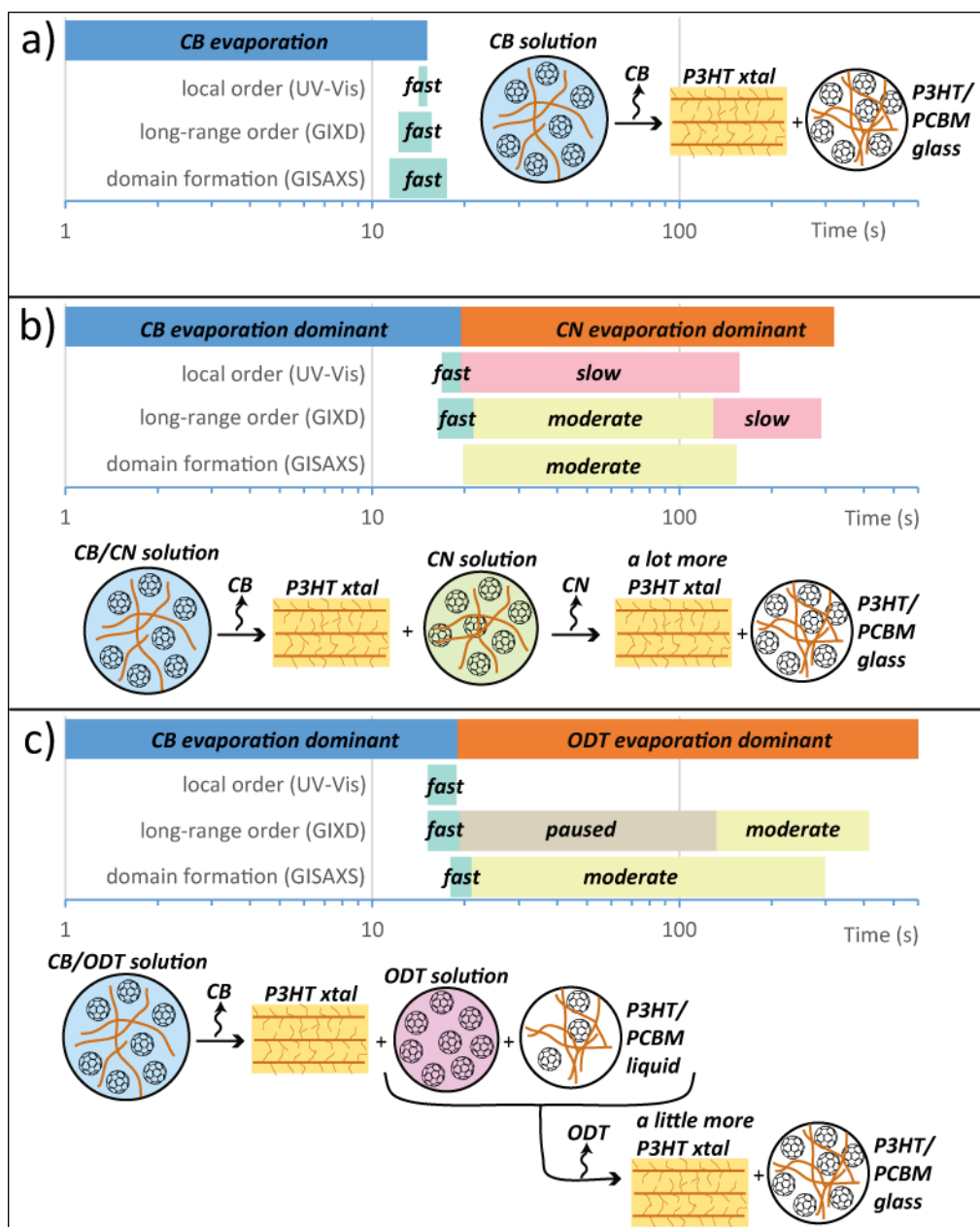


Figure 8. Graphical summary of film solidification measurements for the three P3HT/PCBM formulations studied a) CB only, b) CB with CN additive, and c) CB with ODT. A sequence of how the number and nature of phases progress during evaporation is shown with each data summary.

The table of contents entry should be 50–60 words long, and the first phrase should be bold.

**Synchrotron X-ray scattering measurements of nanoscale structure evolution during the drying of polymer-fullerene photovoltaic films** are described by Richter et al. on pg. XXXX.

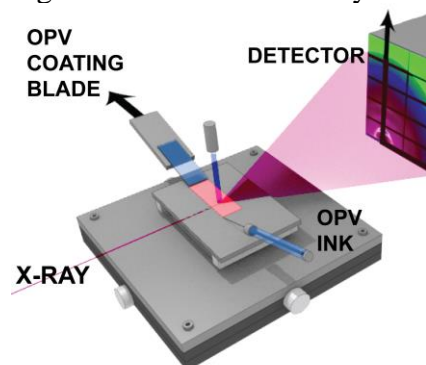
Changes in the number and nature of phases, and the order within them, revealed the mechanisms by which formulation additives promote structural characteristics leading to higher power conversion efficiencies.

### Keyword

C. Author 2, D. E. F. Author 3, A. B. Corresponding Author\* ((same order as byline))

### Title ((no stars))

ToC figure ((Please choose one size: 55 mm broad × 50 mm high **or** 110 mm broad × 20 mm high. Please do not use any other dimensions))



((Supporting Information can be included here using this template))

Copyright WILEY-VCH Verlag GmbH & Co. KGaA, 69469 Weinheim, Germany, 2013.

## Supporting Information

### In-situ Morphology Studies of the Mechanism for Solution Additive Effects on the Formation of Bulk Heterojunction Films.<sup>1</sup>

*Lee J. Richter,\* Dean A. DeLongchamp,\* Kang Wei Chou, Aram Amassian, Eric Schaible, Alexander Hexemer*

#### Supplemental

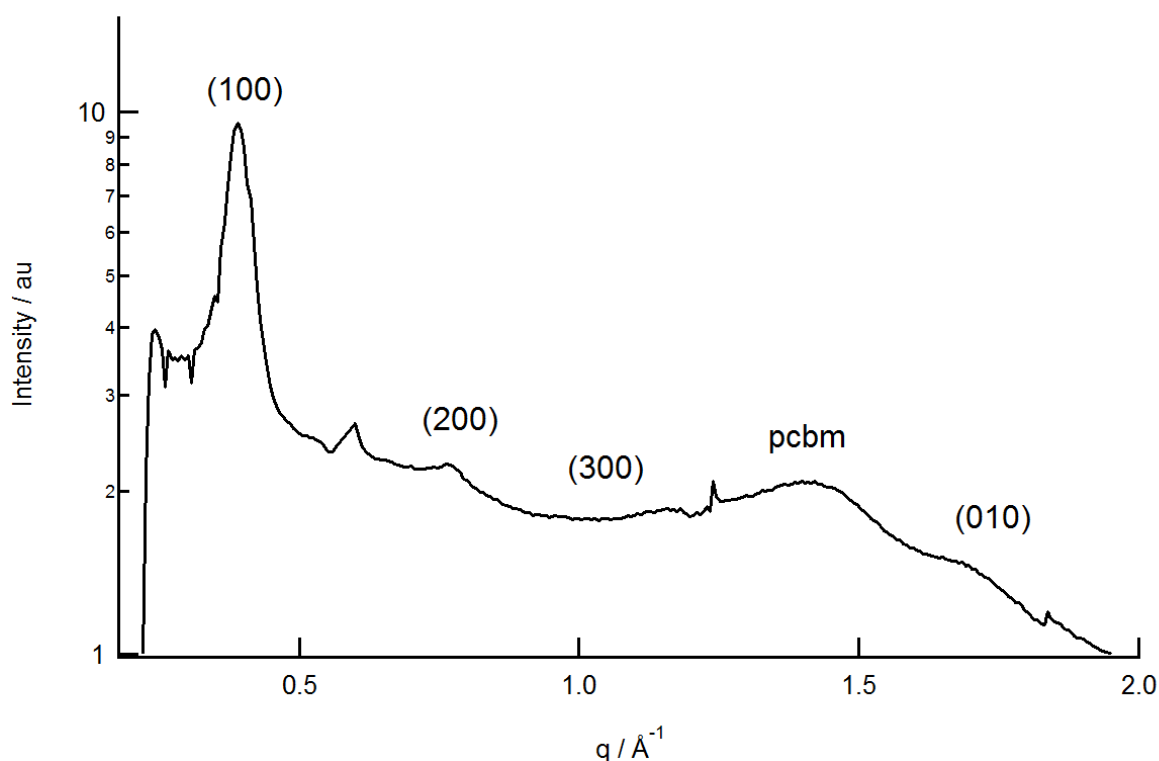


**Figure S0** +/- 15° sector average about  $q_x = 0$  for the additive-free BHJ. Principle diffraction features are labeled. The discontinuities near  $0.6 \text{ \AA}^{-1}$ ,  $1.2 \text{ \AA}^{-1}$  and  $1.8 \text{ \AA}^{-1}$  are artifacts due to the cell structure of the imaging detector.

<sup>1</sup> Official contribution of the National Institute of Standards and Technology; not subject to copyright in the United States.

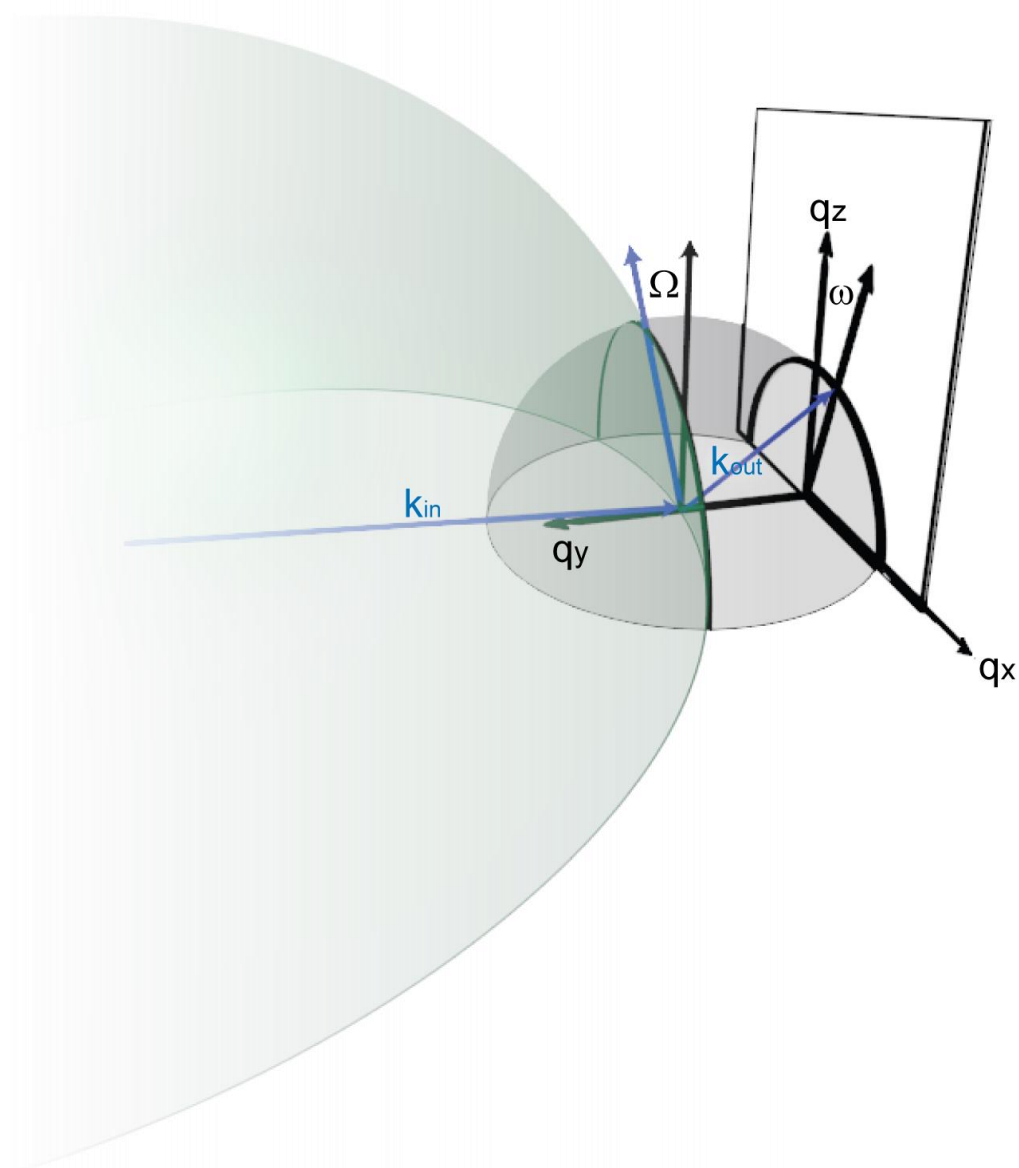


Figure S1. Intersection of the orientation sphere (polar angle  $\Omega$ ) with the Ewald Sphere and the projection onto the image detector (angle  $\omega$ )

Additional support for the interface nucleation hypothesis can be found in the depth profiles of the (100) pseudo pole figure. Below the critical angle (surface sensitive) the isotropic plateau/wings are absent.

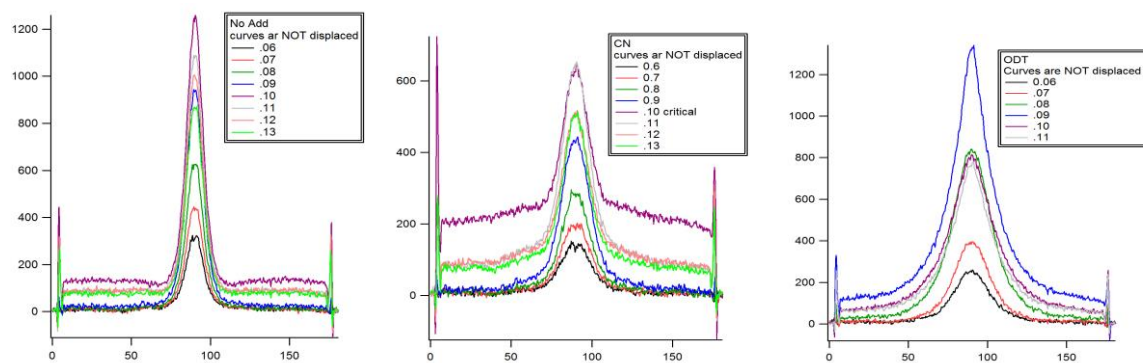


Figure S2 Angle dependent (100) pseudo pole figures for additive-free, CN and ODT additive.

X-axis is uncorrected orientation angle  $\omega$ .

Additional support for the vitrification hypothesis can be found in studies of additive-free BHJs as a function of PCBM loading. Shown in Figure S3 is the P3HT crystallinity: (100) pole figure normalized to film thickness and polymer volume fraction (red open circles), for additive-free films as a function of the PCBM volume fraction. One can see that the polymer crystallinity is essentially independent of PCBM loading until  $\approx 50\%$  mass fraction where it precipitously drops. Also shown in Figure S3 is the T<sub>g</sub> of the blend (black filled symbols), based literature studies.<sup>1</sup> One can see a clear correlation between the composition range where PCBM begins to disorder the polymer and when the film T<sub>g</sub> becomes slightly above the stage temperature (30 °C) as shown in the box.

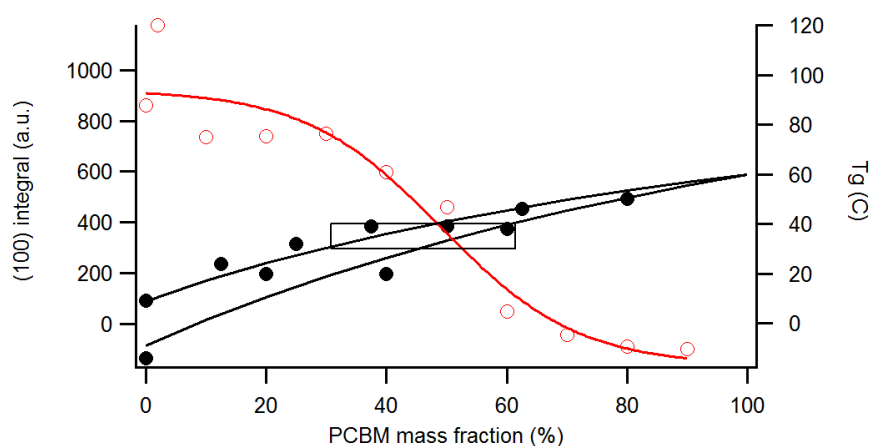


Figure S3 Red: psudeo (100) pole figure as a function of PCBM % mass fraction for additive-free, as-bladed films. Black: T<sub>g</sub> from the literature. Lines are drawn to guide the eye.

In a simple, 2 phase system, the TSI is given by  $TSI \sim (\Delta\rho)^2 \phi(1 - \phi)$  where  $\Delta\rho$  is the difference in scattering length density between the two phases and  $\phi$  is the volume fraction of one phase. If we assume the two phases are crystalline P3HT and a mixed amorphous phase of P3HT, PCBM, and solvent and assume ideal mixing in the mixed amorphous phase, the TSI can be calculated from standard approximations to the x-ray scattering length and the densities of the neat components.<sup>ii</sup> For the 5 component system of crystalline polymer, amorphous polymer, fullerene, solvent and additive, the TSI becomes a function of 3 volume fractions: crystalline polymer ( $\phi_{xtal}$ ), solvent ( $\phi_{cb}$ ), and additive ( $\phi_{add}$ ). Assuming volume conserving mixing, the volume fractions can be calculated from the known pcbm volume fraction of the dry film ( $f_{pcbms}$ ), the dry film thickness ( $t_{dry}$ ), the thickness attributed to the solvent ( $t_{cb}$ ) and additive( $t_{add}$ ) and the (100) pseudo pole figure with one unknown scale factor:

$$\begin{aligned} \phi_{cb} &= \frac{t_{cb}}{t_{cb} + t_{add} + t_{dry}} \\ \phi_{add} &= \frac{t_{add}}{t_{cb} + t_{add} + t_{dry}} \\ \phi_{pcbms} &= f_{pcbms} \frac{t_{dry}}{t_{cb} + t_{add} + t_{dry}} \\ \phi_{xtal} &= C_{xtal}(100)_{pole\ figure} \\ 1 &= \phi_{xtal} + \phi_{amor} + \phi_{pcbms} + \phi_{cb} + \phi_{add} \\ f_{pcbms} = 0.42 &= \frac{\phi_{pcbms}}{\phi_{xtal} + \phi_{amor} + \phi_{pcbms}} \\ \Delta\rho &\propto \left(1 - \frac{\phi_{amor} + \alpha \phi_{pcbms} + \beta \phi_{cb} + \gamma \phi_{add}}{\phi_{amor} + \phi_{pcbms} + \phi_{cb} + \phi_{add}}\right) \\ TSI &\propto \frac{\left(\phi_{add} - \gamma \phi_{add} + \phi_{cb} - \beta \phi_{cb} + f_{pcbms}(-1 + \alpha)(-1 + \phi_{add} + \phi_{cb})\right)^2 \phi_{xtal}}{\phi_{xtal} - 1} \end{aligned} \quad Eq. S1$$

	Mol formula	Density	SLD (x10 <sup>5</sup> )	SLD Ratio
P3HT	C11H14S	1.12	1.03	

PCBM	C72H14O2	1.60	1.38	$\alpha=1.34$
CB	C6H5Cl	1.11	0.98	$\beta=0.95$
CN	C10H7Cl	1.19	1.05	$\gamma=1.02$
ODT	C8H18S2	0.97	0.91	$\gamma=0.88$

Shown in Figure S4 is the raw (100) psuedo pole figure and *in-situ* film thickness and the raw TSI and *in-situ* film thickness for CN additive films. The GIWAXS and GISAXS were performed during different runs and there is a clear difference in the film drying kinetics, reflected in the position of the thickness kink due to cb removal and the final removal of CN. In order to correct for the drying, the GIWAXS time axis was shifted to align the position of the kink and scaled to align the drying of the CN. Also shown in Figure S4 are the resulting time dependent volume fractions and the scaled GIWAXS results. The results of the predicted TSI (Eq. S1 with only 2 adjustable parameters:  $C_{\text{xtal}}$  and over scale) are also shown. The simple 2 phase describes the data very well.

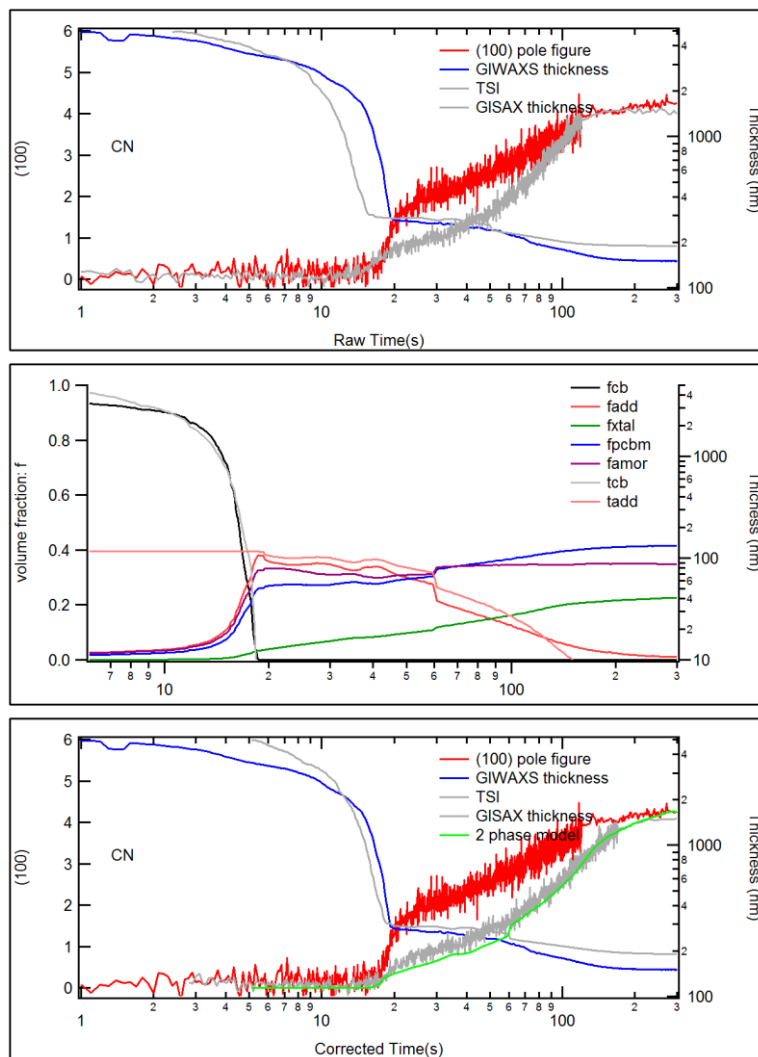


Figure S4 development of 2 phase model for CN additive results

Shown in Figure S5 is the raw and time corrected data for films containing ODT as additive. Also shown is the prediction from Eq. S1. Clearly the simple 2 phase model fails completely to describe the evolution of the TSI. The early time TSI is much stronger than expected based on the average contrast of the ODT diluted mixed amorphous phase. For a 3 phase system, Wu has shown that the TSI is proportional to  $\Delta\rho_{12}^2\phi_1\phi_2 + \Delta\rho_{13}^2\phi_1\phi_3 + \Delta\rho_{23}^2\phi_2\phi_3$ . Given the marginal solubility of P3HT in ODT we have developed a 3 phase model consisting of P3HT crystal, mixed amorphous (amorphous polymer, PCBM, cb) and additive (PCBM and ODT). The PCBM partitions between the additive and mixed amorphous phases as:

$$\phi_{pcb}^{amor} = \phi_{pcb} \frac{k\phi_{amor}/\phi_{add}}{1+k\phi_{amor}/\phi_{add}}.$$

This introduces one more parameter, the partition coefficient of PCBM between the mixed amorphous and odt phases. As shown in S5, the three phase model describes the data very well, with a partition coefficient of 1.9 which corresponds to a weak preference of the PCBM to reside in the polymer phase.

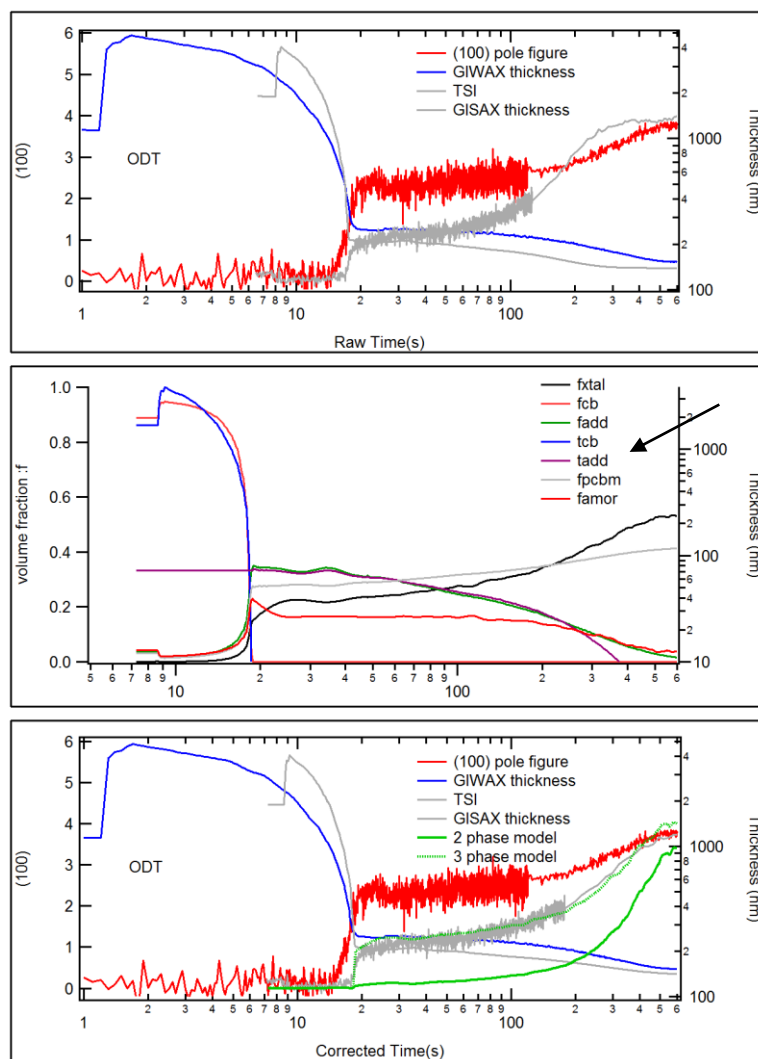


Figure S5 development of 2 phase model and 3 phase model for ODT additive results

<sup>i</sup> Ngo, T. T.; Nguyen, D. N. *Adv. Nat. Sci. Nanosci. Nanotechnol.* **2012**, *3*; Kim, J. Y.; Frisbie, C. D. *J. Phys. Chem. C* **2008**, *112*, 17726–17736.

<sup>ii</sup> Ro, H. W.; Akgun, B.; O'Connor, B. T.; Hammond, M.; Kline, R. J.; Snyder, C. R.; Satija, S. K.; Ayzner, A. L.; Toney, M. F.; Soles, C. L.; DeLongchamp, D. M. *Macromolecules* **2012**, *45*, 6587–6599.